

Production and performance of the InFOC μ S 20–40 keV graded multilayer mirror

F. Berendse

Department of Astronomy, University of Maryland at
College Park and NASA Goddard Space Flight Center,
Greenbelt, MD 20771

berendse@astro.umd.edu

S.M. Owens, P.J. Serlemitsos, and J. Tueller

NASA Goddard Space Flight Center, Greenbelt, MD, 20771

K.-W. Chan, Y. Soong, and H. Krimm

Universities Space Research Association and NASA
Goddard Space Flight Center, Greenbelt, MD, 20771

W.H. Baumgartner

Department of Astronomy, University of Maryland at
College Park and NASA Goddard Space Flight Center,
Greenbelt, MD 20771

Y. Ogasaka, K. Tamura, T. Okajima, Y. Tawara and K.

Yamashita

Department of Physics, Nagoya University, Furo-cho,

Chikusa-ku, Nagoya 464-8602, Japan

K. Misaki and H. Kunieda

Institute of Space and Astronautical Science, 3-1-1

Yoshinodai, Sagamihara, Kanagawa 229-8510, Japan

The International Focusing Optics Collaboration for μ Crab Sensitivity (InFOC μ S) balloon-borne hard x-ray telescope incorporates graded multilayer technology to obtain significant effective area at energies previously inaccessible to x-ray optics. The telescope mirror consists of 2040 segmented thin aluminum foils coated with replicated Pt/C multilayers. A sample of these foils was scanned using a pencil-beam reflectometer to determine multilayer quality. The results of the reflectometer measurements demonstrate our capability to produce a large quantity of foils while maintaining high-quality multilayers with a mean Nérot-Croce interface roughness of 0.5 nm. We characterize the performance of the complete InFOC μ S telescope with a pencil beam raster scan to determine the effective area and encircled energy function of the telescope. The measured effective area of the complete telescope is 78, 42 and 22 cm² at 20, 30 and 40 keV, respectively. The measured encircled energy fraction of the mirror has a half-power diameter of 2.0 ± 0.5 arcmin (90% confidence). The mirror successfully obtained an image of the accreting black hole Cygnus X-1 during a balloon flight in July, 2001. The successful completion and flight test of this telescope demonstrates that graded-multilayer telescopes can be manufactured with high reliability for future x-ray telescope missions such as Constellation-X. ©2002 Optical Society of America

OCIS codes: 110.6770, 110.7440, 310.1860, 340.740, 340.7470, 350.1270

1. Introduction

X rays are produced by some of the most energetic and exotic celestial objects such as supernovae, neutron stars, black holes, active galactic nuclei, and gamma-ray bursts. Hot plasmas found in these objects produce x rays and gamma rays from a variety of thermal and nonthermal emission mechanisms. Spectra, images, and timing analysis of these photons provide astronomers the ability to diagnose such things as ionization states, temperatures, elemental abundances, and magnetic fields of the plasmas that produce them. Unlike optical light, x rays are focused by grazing-incidence reflection off of surfaces coated with a smooth layer of high-density material. The High Resolution Imager on the Einstein Satellite, launched in 1978, was the first to employ x-ray-focusing optics.¹ Observatories continue to employ grazing incidence optics to explore the x-ray universe up to energies of 15 keV, including ASCA, BeppoSAX, Chandra, XMM, and Astro-E.²⁻⁶

Although celestial objects typically emit photons throughout the entire x-ray and into the gamma-ray regime, past and current x-ray observatories have focused primarily on studying x rays below 15 keV. Current and near-future observatories capable of studying the x-ray sky above 15 keV (BeppoSAX, RXTE, INTEGRAL, HETE-2) employ non-focusing techniques such as coded masks or grazing-incidence concentrators to improve sensitivity and provide imaging capability.^{3,7-9} These missions do not use grazing-incidence optics because the critical angle for total external reflection of materials decreases with increasing energy. Therefore, mirrors designed for the hard x-ray band would require more reflecting surface (and thus more weight) and either longer focal lengths or smaller geometric area. Such a mirror has been recently implemented by the HERO collaboration to extend grazing-incidence

optics capabilities to 50 keV.¹² We feel, however, that an alternative technology is necessary to keep the mirror lightweight – an important consideration for future space-based observatories. Periodic multilayers have long been known to increase the reflectivity of surfaces above the critical angle, but are very limited in the range of energies they can reflect efficiently. It wasn't until the development of graded multilayers and the realization of their potential in astronomical applications that an alternative to grazing-incidence optics became available.^{10,11} Graded multilayers are the method of choice of this work, the HEFT balloon-borne telescope, and Constellation-X.^{13,14}

The International Focusing Optics Collaboration for μ Crab Sensitivity (InFOC μ S) is a balloon-borne hard x-ray telescope built jointly by NASA's Goddard Space Flight Center (GSFC), Nagoya University, Japan's Institute of Space and Astronautical Science (ISAS), and the University of Arizona. It is an 8 m focal length telescope with an altitude-over-azimuth pointing system. It is the first to employ two key technologies to improve imaging and sensitivity in the hard x-ray regime. The first is a mirror system composed of thin aluminum foils coated with a graded multilayer to provide broad-band reflectivity and a wide field of view at incidence angles as large as 0.3°. Our collaboration has proven that this technology is a promising way to build a hard x-ray telescope mirror.¹⁵ The other breakthrough technology is the focal plane detector, which is a solid-state detector composed of Cadmium Zinc Telluride (CZT). CZT is capable of achieving 100% efficiency at 20–100 keV with a thin detector – thus reducing the instrument noise and increasing the sensitivity of the instrument.¹⁶

The InFOC μ S mirror system, shown in Fig. 1, was modeled after the Astro-E mirror system. The mirror has an outer diameter of 40 cm, an inner diameter of 12 cm and a focal

length of 8 m. The primary and secondary mirror each contain 255 nested shells in a conical approximation of a Wolter I configuration. Each shell is composed of 4 quadrants of a 0.152 mm thick aluminum substrate formed into a conical approximation to the ideal parabolic or hyperbolic shape. This significantly reduces the complexity and cost of forming the foils. At a focal length of 8 m, this approximation produces an image with a half-power diameter of 15 arcsec— small compared to the effects limiting the image quality of the mirror to be discussed later in this paper. The segments are held in place by 26 precision alignment bars radially spanning the top and bottom of each mirror quadrant. The angle of incidence of an on-axis ray, measured from the mirror plane, varies from 0.1° for the innermost shell to 0.35° for the outermost shell.

Section 2 of this paper describes the design, deposition, and results of the individual foil multilayers. Section 3 outlines the calibration and performance of the complete InFOC μ S mirror. Section 4 summarizes our results.

2. The InFOC μ S multilayers

A. Design and deposition

Each foil segment is coated with a Pt/C multilayer in order to achieve the desired 20–40 keV bandwidth of the mirror. Periodic multilayers are only efficient at reflecting a very narrow energy band at a given incidence angle. To achieve broad-band reflectivity with periodic multilayers one would need many reflecting surfaces each tuned to a specific narrow energy range for an on-axis x ray. Such a design would provide very little off-axis reflectivity. In a Wolter type-I system, if an off-axis X ray intersects the primary mirror at an angle $\alpha + \beta$ where α is the angle of incidence of an on-axis x ray, it will intersect the secondary mirror

at an angle $\alpha - \beta$. Periodic multilayers tuned to a specific energy on axis could not possibly reflect off-axis x rays of any energy off both the primary and secondary with high efficiency. Therefore periodic multilayers are not the desired solution for a telescope designed to have significant effective area over broad energy range. Grading the thickness of the layers vs. depth provides the desired broadband reflectivity.¹⁷ By decreasing the bilayer thickness from vacuum to substrate, the lower energy x rays are efficiently reflected by the layers closest to vacuum. The higher energy x rays, which penetrate deeper into the multilayer stack, are reflected by the layers closest to the substrate.

Multilayers for two of the four quadrants were coated at Nagoya University by DC magnetron sputtering. Foils used in these quadrants were first prepared by replicating a 200.0 nm platinum layer at GSFC. This technique, first developed for the Astro-E telescopes, begins by depositing the platinum onto a smooth (0.3 nm RMS roughness) glass mandrel. The layer is transferred to the foil by coating the mandrel with an epoxy, then placing the foil onto the mandrel and allowing the epoxy to cure in an oven. When the foil is removed, the platinum layer sticks to the foil and replicates the smoothness of the mandrel. This replication process compensates for the μm to mm-scale waviness introduced when milling and forming the aluminum foils.¹⁸ The bilayer thickness for these foils varies in discrete steps as a function of depth in a "stepped block" configuration. The deposition design, process and results of these two quadrants are described in a separate paper.¹⁹ The remainder of the this section will focus on multilayers of the two quadrants fabricated at GSFC.

The multilayer design of the GSFC foils employs a smooth power law transition of layer thickness. We followed the design procedure of Joenssen *et al.* to determine the bilayer

thickness d^{20}

$$d = a(i + b)^{-c} \quad (1)$$

where i is the bilayer number starting from 1 at the layer closest to vacuum and a , b and c are free parameters.²⁰ We adopt values of $b = 0.5$ and $c = 0.27$ for this work. We determined a by first determining the characteristic energy each foil would reflect most efficiently. This characteristic energy E changes linearly from 38 keV for the innermost foils to 18 keV for the outermost foils to cover the desired bandpass of the mirror. From this characteristic energy, a nominal bilayer spacing d_0 can be defined for each foil by satisfying the first-order Bragg condition for a periodic multilayer at the angle of incidence of an on-axis x ray α

$$\frac{hc}{E(\text{keV})} = 2d_0 \sin \alpha \left[1 - \frac{2(\Gamma \delta_{Pt} + (1 - \Gamma) \delta_C)}{\sin^2 \alpha} \right]^{1/2} 0.5 \quad (2)$$

where Γ is the ratio of Pt layer thickness to total bilayer thickness and δ is the deviation from unity of the real part of the complex index of refraction $n = 1 - \delta + \beta$. Setting the parameter a equal to $1.5d_0$ places the maximum reflectivity near the design energy. Adopting a value of $\Gamma = 0.45$, we can express the thickness of each layer

$$\begin{Bmatrix} d_{Pt} \\ d_C \end{Bmatrix} = \begin{Bmatrix} 0.45 \\ 0.55 \end{Bmatrix} 1.5d_0(i + 0.5)^{-0.27}. \quad (3)$$

The number of layers deposited on each foil is also a free design parameter. The reflectivity of the multilayer increases as a function of number of layers deposited until it saturates due to absorption by the platinum. It was also desirable to minimize the number of layers to mass produce foils in a timely manner. Optimizing the number of layers on each foil involves depositing enough layers to just reach the saturation point. We adopt a coarse optimization of the number of layers by choosing 15 bilayers for shells 1-50 (1 is the innermost shell), 30

for shells 51-100, 40 for shells 101-150, 50 for shells 151-200 and 60 for shells 201-255. Fig. 2 is a set of simulated reflectivity curves of foils at three different radii which demonstrates the high reflectivity of the inner foils due to an on-axis angle of incidence close to the critical angle of platinum. At medium radii, the foils still can cover the entire energy range but have numerous peaks and valleys. The outermost foils are designed to reflect the lowest energies and do not reach the high-energy bandpass. Only by adding the contributions of all the foils can we obtain constant effective area over the entire 20–40 keV range.

Multilayers were placed onto foils at GSFC by depositing all bilayers, rather than a single layer, onto the mandrel – then replicating the entire multilayer onto the foil. In order to produce multilayers for 1020 foils in an efficient manner, we implemented an automated deposition process which can handle up to six glass mandrels in a single deposition run. A schematic of the deposition chamber is given in Fig. 3. Each mandrel is placed on its own rotation stage controlled by a stepper motor. Two DC magnetron sputtering sources with 8×2 inch targets are at opposite sides of the chamber depositing simultaneously onto two different mandrels. The mandrels are rotated in front of the targets at a variable rate to control the layer thickness sputtered onto the mandrel. We compensated for a nonuniformity in sputtering rate as a function of vertical distance by placing a mask immediately in front of each mandrel. This allowed the top and bottom of the mandrel to be exposed to the target for a longer time during mandrel rotation. The platinum and carbon targets were operated at powers of 57 W and 500 W, respectively. The ambient pressure in the chamber before sputtering was 1.0×10^{-5} Torr. Argon was introduced at a pressure of 7.5×10^{-4} Torr during sputtering. After multilayer deposition, an additional 50–200 nm layer of platinum was sputtered onto the mandrel using a hollow cathode sputtering chamber. We found that

this additional platinum eased the transfer of the multilayers to the aluminum substrate during replication.

B. Measurement and results

In order to ensure that we were obtaining the desired multilayer structure, we obtained reflectivity measurements for a sample of foils. We used a short beamline reflectometer shown in schematic in Fig. 4. The x rays were generated with a Rigaku UltraX rotating anode generator with a copper target. The source generated a $3\text{ mm} \times 0.3\text{ mm}$ spot size at the target. The x rays were then filtered by a Ge(111) double-crystal monochromator tuned to reflect the Cu $\text{K}\alpha_1$ line at 8.047 keV. Even though the beamline in this configuration was only about 1 m, a $120\text{ }\mu\text{m}$ tantalum pinhole placed at the front of the sample chamber was sufficient to filter out the Cu $\text{K}\alpha_2$ line. In order to minimize stresses on the foil during testing, we allowed the foil to lean freely against a vertical surface at the point where the x-rays intersect the foil. This kept the reflected beam in the same horizontal plane as the incident beam. The detector used in the reflectometer was an Amptek 100-CZT model CdZnTe detector with a $3\text{ mm} \times 3\text{ mm}$ area at a distance of 780 mm from the center of the foil sample. Both the foil sample and detector were rotated in a θ - 2θ manner in steps of 0.005° in θ .

The multilayers were characterized by fitting the reflectivity scan to a simulated reflectivity curve generated by the software package IMD written by Windt.²¹ Five parameters were free to vary in this fitting procedure: the top and bottom platinum layer thicknesses, the top and bottom carbon layer thicknesses, and the Nérot-Croce RMS interface roughness between at each boundary.²² The power law index of the multilayer was frozen at its design value of -0.27. Varying the top and bottom layer thicknesses while keeping the power law in-

dex frozen is a more tangible way of varying the value b in Eq. (1). The interface roughnesses of both boundary types were assumed to be equal *i.e.* $\sigma_{Pt/C} = \sigma_{C/Pt}$. To help the software arrive at a best fit, we performed a preliminary fit by setting the carbon layer thicknesses equal to 1.22 times the platinum layer thicknesses. We then freed the carbon layer thicknesses and performed a second fit. We found very similar results if the preliminary fit was done with a variable carbon layer thicknesses. Results from a fit to a typical reflectivity scan are shown in Fig. 5.

78 of the 1020 foils produced at GSFC¹ were characterized in this manner. Of those foils measured, 68 produced fits which were qualitatively good enough to quantify the layer thicknesses and interface roughness of the multilayer. This sample was split into two different radius ranges, 7.63–9.16 cm (inner foils) and 12.91–19.54 cm (outer foils). The most important parameter of this fit is the interface roughness, as it determines how efficiently the multilayer will reflect x rays at all energies. Fig. 6 shows the interface roughness increasing from a mean value of 0.45 ± 0.07 nm for the sample of inner foils to 0.60 ± 0.14 nm for the sample of outer foils. A Kolmogorov-Smirnov test gives a probability of 6×10^{-4} that these distributions are samples of the same parent distribution. To show that this is not a bias of fitting or measurement technique, we plot in Fig. 7 two sample foils, one from each of the two radius ranges. In these figures, we compare the best-fit model for that foil to a model with a frozen roughness equal to the mean roughness of the other sample set. All other parameters were allowed to vary to obtain a best fit. We believe the correlation between foil radius and interface roughness is primarily due to buildup of interface roughness as a function of the number of layers deposited onto the foil.

In previous work based on diffuse scatter measurements of a sample foil, we found

that the interface roughness is entirely geometric roughness – *i.e.* the boundaries between the layers are well-defined but rough as opposed to layer boundaries that are not well-defined due to diffusion of one material into the other.²³ The diffuse scatter arising from this roughness is approximately 0.5% of the image flux. For the faint images that InFOC μ S will be observing, where the signal-to-noise ratio will be relatively low, the noise contribution from diffuse scatter will not be significant compared to other contributions.

The process of depositing a great number of multilayers within a short period of time and producing multiple sets of multilayers within one deposition chamber places unique challenges in ensuring the proper thicknesses are deposited. A drift in the deposited thickness over time will cause individual foils to efficiently reflect a different range of energies than originally intended. This could have drastic consequences on the resulting effective area over the desired energy range. Our measurements of the top bilayer thicknesses in Fig. 8 show that our mean fitted to ideal bilayer thicknesses was 1.02 ± 0.07 . Of the samples measured, 62% had a fitted bilayer thickness within 5% of their designed thickness. A tendency to deposit thicker platinum layers than designed was detected after monitoring the first 30 foils. Based on this, an adjustment was made to the mandrel rotation rate in front of the platinum target. Measurements of subsequent foils revealed this systematic error had been corrected. The spread in fitted vs. designed bilayer thickness corresponds to a thickness repeatability of ± 0.7 nm. This must be attributed to a drift in the sputter rate over a deposition run. We can rule out a large thickness variability from layer to layer which would give the peaks in the reflectivity curve that no longer appear at regular incidence angle intervals.

We point out that these layer thicknesses are only a best fit of an ideal power-law multilayer to our measurement data. The fits of all our foils to a power-law multilayer all

have values of χ^2 per degree of freedom much greater than 1. The fits are poorest at the highest angles of incidence where the reflectivity comes primarily from the thin layers at the bottom of the multilayer stack. Therefore, it is likely that our determination of the bottom thickness is biased by the fit of the top layer thickness. We see a high correlation between the best-fit bottom and top layer thicknesses in both platinum and carbon which we attribute to this bias.

We find only a slight correlation between the fit of the platinum and carbon top layer thickness ratios shown in Fig. 9. A linear regression fit gives a slope of 0.27 and a linear correlation coefficient of 0.38. This result rules out common sources of change in deposition rate as the dominant cause of the variation of layer thickness from its design value. Such common sources include variations in the distance between the mandrel and the sputtering target and pressure of the argon sputtering gas. This also rules out any systematic error in the reflectivity measurement due to misalignment of the foil or an offset in the beam energy used in the reflectometer.

3. Complete mirror tests

A. Pencil-beam raster scan

In order to measure the effective area and image quality of the complete mirror, we used a pencil beam to scan the mirror. This was the most feasible way of measuring the mirror given that the long beamline facility at GSFC cannot accommodate an 8 m focal length mirror. This setup, shown in Fig. 10, uses a portable x-ray source mounted onto two large translation stages, each with 60 cm throw and 10 μm resolution. One translation stage moves the source in a vertical direction, the other moves the source in a horizontal direction perpendicular to

the optical axis. The pitch and yaw of the pencil beam are controlled by two precision tilt stages with 0.1 arcmin resolution.

The x-ray source is an Oxford 5011 x-ray tube with a tungsten anode. The source intrinsically produces a spot size of 105 x 130 microns. We operated the source at 50 kV and 0.75 mA. In order to remove the characteristic Tungsten lines, we placed a 0.135 mm thick Ni filter in front of the source. This filter was placed directly in front of the collimating pinhole at the end of a 70 cm collimation tube. The pinhole is a tungsten pinhole 100 microns in diameter and 3 mm thick. All measurements were done in ambient atmosphere. The photon count rate of the direct beam in a 1 atm environment at a distance of 8.5 m was 4000 photons s^{-1} at 20–50 keV. The scan started at the top of the mirror, translating the source at a rate of 1–2 cm s^{-1} in the horizontal direction, then stepping 2 mm down in the vertical direction and scanning horizontally in the other direction. We typically collected a total of 10^5 photons in a complete raster scan and covered about 5% of the geometric area of the mirror.

In order to get an accurate representation of how the mirror behaves, it is necessary to account for any systematic effects introduced by the raster-scan system. We found two such systematic effects that must be accounted for in our analysis of the image quality. The first is that there is a smooth change in the pitch or yaw as the source travels along the vertical or horizontal stages, respectively. Over the 40 cm diameter of the mirror, this change is about ± 0.33 arcmin. This is equivalent to illuminating the mirror with a source at a distance of about 2 km rather than at an infinite distance. All of the ray trace simulations presented in this paper will simulate sources at this finite distance.

The other systematic effect is the divergence of the beam coming from the x-ray source. Taking the source size and the collimating pinhole as limits, the beam has a divergence of

about 1 arcmin. As this is comparable to the image spot produced by the mirror, it must be taken into account. This divergence also reduces the measured on-axis effective area by about 2–4% by sampling some off-axis angles. We do not believe a similar reduction will occur in the off-axis measurements. Unlike the on-axis case, when the beam is off-axis the mean effective area over the range of off-axis angles sampled by the beam is approximately the effective area sampled by the center of the beam.

The determination of the mirror image quality is also affected by the pixel size of the CdZnTe focal plane detector in the InFOC μ S telescope. The pixels are 2.1 x 2.1 mm in size, which is about 54 arcseconds in angular size. This is comparable to the expected HPD of the mirror. Rather than trying to account for these systematic effects in our actual image through complicated deconvolution techniques, we take a more straightforward approach by folding these systematic effects into our ray-trace simulations and comparing to the measured data.

One of the most important steps in determining the performance of the mirror using the raster scan system is aligning the pencil beam with the x-ray axis of the mirror. The procedure we used is to first obtain a coarse alignment by placing the collimator at the center of the mirror and adjusting the beam to hit the center of the detector. The coarse alignment was then refined by scanning the mirror with the x-ray source along a radius close to the middle of a quadrant. (We could not align it exactly with the middle because an alignment bar was at the middle of each quadrant.) We then adjusted the pitch (or yaw) for that particular quadrant to maximize the throughput. This procedure was repeated for a neighboring quadrant to adjust the beam yaw (or pitch).

B. Full mirror performance

The on-axis and off-axis effective area and the image quality of the full telescope were determined using the raster scan setup described above. During these tests, both the detector and mirror were mounted on the InFOC μ S telescope in a horizontal configuration. However, when in operation, the telescope is usually operated in a nearly vertical position. We cannot rule out that the performance of the mirror will change slightly in the vertical configuration, however no degradation in mirror performance has been reported between pre-flight calibration tests on the ground and in-flight calibration tests in space for mirrors using the same foil technology and mirror housing.

The on-axis effective area measured with the raster scan is shown in Fig. 11. Two predictions of the effective area are included in this figure. The first is simply the sum of each foils' reflectivity multiplied by the geometric area of that foil. The second is a prediction based on ray tracing with a distribution of slope errors. This distribution is the same as the distribution of slope errors that could empirically explain the reduction in effective area of the Astro-E telescope mirrors.²⁴ This distribution is a Gaussian distribution with a mean value of 0° and a standard deviation of $0.12^\circ R^{-1.3}$, where R is the reflectivity of the foil. Both simulations in Fig. 11 assume an interface roughness of 0.5 nm. The slope errors of the foils cause a significant reduction in measured effective area by scattering x rays into the backs of adjacent foils. This foil waviness is primarily on the macroscopic scale and is introduced during replication of the multilayers onto the foils and insertion of foils into the mirror housing.

The mandrels used for replication of the multilayers were cylindrical in shape rather than

conical. Although this could be solved by simply using a conical mandrel, the epoxy used in the replication process is thick enough to introduce stress to the foils. Deviations from flatness introduced by the process are on the order of $\pm 1\mu\text{m}$ over an 80 mm spatial scale.²⁵ We have also observed that both platinum and carbon are sputtered under compressive stress which, when replicated, causes the foils to increase their radius of curvature. This stress results in a 4–8% increase of the radius of curvature of the foils after replication which could introduce slope errors if placed at their original radius. To minimize the effect this radius increase would have on the final image quality, as many GSFC foils as possible were placed at their modified radius. Similar increases in radius were observed with the Nagoya foils but were placed at their original radii.

The placement of the foils within the mirror housing also can cause the foils to bend. Each foil is held within the mirror by 13 alignment bars on the top and bottom of each mirror quadrant. The alignment bars are etched with trapezoid-shaped grooves which hold the ends of the foils. These grooves are designed to be wider than the thickness of the foils to prevent binding during foil installation into its designed slot. There are two issues limiting the image quality one can obtain with this design. First, the machining of these grooves leaves rounded corners at the bottom of the groove which causes the foil edge to be in the wrong position leading to a slope error for the entire foil. Second, these bars are the only mechanism for holding the individual foils in place, so they must be adjusted to prevent the foils from moving. To do this, the alignment bars are positioned to alternate between supporting the back and the front of the foil. These alignment bars must also be adjusted to produce the best overall image and not necessarily the best image for each set of foils. While producing the best overall image, stresses are placed on individual foils which also

contribute to slope errors.

The field of view of the telescope is limited by vignetting caused by the small spacing between the thin foils necessary to ensure that no stray light reaches the focal plane. To measure the field of view, we mounted the entire pencil beam setup onto two perpendicular tilt stages and adjusted the tilt from the on-axis position in the azimuthal direction (i.e. within the horizontal plane). We define the field of view as the full width of off-axis angles that produce at least 50% of the on-axis effective area. We have measured the mirror effective area at five off-axis positions and interpolate between the measurements using a cubic spline, shown in Fig. 12. The field of view of the telescope in the azimuthal direction is 12.6, 10.5 and 9.3 arcmin at 20, 30 and 40 keV, respectively. The results in the elevation direction were slightly smaller-- 9.0, 10.4, and 8.6 arcmin at 20, 30 and 40 keV, respectively.

An on-axis image produced by a pencil-beam raster scan of the full mirror is shown in Fig. 13. Each pixel in the image corresponds to an actual pixel on the CdZnTe detector. The focus is intentionally placed off the center of the detector to avoid pixels with nonuniform spectral response and detection efficiency on the right side of the detector. The peak in this image is above 12000 counts. The highly asymmetric appearance of the image can be attributed to binning of an image not centered at the center of a pixel.

We quantify the image quality of the mirror by fitting the encircled energy fraction (EEF) of a ray-trace model to the image EEF. The ray-trace simulations simulate a finite source distance of 2 km and were binned into 12 arcsec pixels. The image quality of the ray trace model was modified by changing the distribution of scattering angles as the rays are reflected from each foil. This is equivalent to changing the width of the gaussian distribution of foil slope errors. The diverging beam is accounted for by convolving the image with a 1

arcmin FWHM gaussian. The image is then centered at the centroid of the actual image and rebinned into 54 arcsecond bins to simulate the detector. Fig. 14 show the EEF of the actual image at different energies and ray trace models varying in image quality. Each model is labeled by the half-power diameter (HPD) of the mirror before accounting for systematic effects of the pencil-beam raster scan. The most probable HPD of the mirror based on this measurement is about 2.0 arcmin. We can rule out with 90% confidence a HPD outside the range of 1.5–2.5 arcmin.

The entire InFOC μ S telescope was flown on a balloon flight from Palestine, TX on July 6, 2001 at 1:10 UT. The balloon attained a float altitude of 38.1–39.0 km corresponding to 3 g/cm² residual atmosphere. Atmospheric transmission of x rays at this altitude range from 5% at 20 keV to 15% at 40 keV from a source at 90° elevation. The balloon stayed at float altitude for 3.9 hours. The black hole candidate Cygnus X-1 (Cyg X-1) was chosen as a calibration target. We were able to successfully observe Cygnus X-1 and will present the results of that observation in a separate paper.

4. Discussion and Conclusion

The InFOC μ S mirror demonstrates that multilayer thin foil optics are a very promising way to produce imaging capability and increased sensitivity for future space-based and balloon-based missions above 15 keV. Two achievable improvements in the mirror could make this capable of achieving 1 arcmin imaging and larger effective area up to energies of 100 keV. The first is decreasing the interface roughness between layers and the second is improving the slope errors introduced by the replication process and fitting the foils into the mirror housing.

Our multilayer deposition process is capable of consistently achieving average interface roughnesses of 0.45–0.6 nm from the inner to the outer foils. However, our best foils achieved an interface roughness of 0.35–0.4 nm, so there is room for improvement in this area. The most probable cause of this difference in roughness is greater roughness buildup on the outer foils which have more bilayers. However, we cannot rule out a degradation in layer thickness quality during a deposition run. The deposition chamber can hold six mandrels, labeled 1–6 in a counterclockwise manner. The chamber deposits layers first onto mandrels 1 & 4 simultaneously, then 2 & 5, then 3 & 6. Mandrels 1 & 4 were the smallest mandrels, and thus designed for the innermost foils while 3 & 6 were the largest. Any contribution to the layer roughness by the deposition process which increases slowly over a deposition run would manifest itself as a systematic increase in roughness vs. foil radius. Also, the mandrels heat up during the deposition process. The greater number of layers deposited onto the outer foils could exacerbate any heat-related contributions to the interface roughness. Decreasing the roughness of all multilayers to 0.4 nm would increase the effective area of the mirror by 10% at 30 keV and 12% at 40 keV.

The slope errors in the foils limit both the effective area and the image quality of the telescope. In our ray-trace modeling of the mirror, we have used the same distribution of slope errors as those used in Astro-E mirror simulations, yet the reduction in effective area of the InFOC μ S mirror was 40–65% compared to a reduction in effective area of 30% for the Astro-E mirror. The reduction in effective area may appear to be different in origin from the Astro-E mirror because it is energy dependent. However, we point out that the reflectivity of the telescope changes with radius. The outer foils, which have higher opening angles between foils, suffer the least from slope errors which cause scattered x rays to hit the backs

of neighboring foils. These foils also do not efficiently reflect the highest end of the energy bandpass. Therefore, the lower-energy x rays will have lower fractional losses as a result of slope errors than the higher-energy x rays.

We can improve these slope errors in two ways. We have observed during our foil production process that we can reduce the stress induced by the Pt/C multilayer by depositing a 5–10 nm layer of gold, instead of platinum, onto the mandrel after multilayer deposition. This reduces the observed radius of curvature change to 1.3% while still providing a good buffer layer needed for the replication process. The trapezoid shape of the alignment grooves can also be improved. We can eliminate the rounded corners by making the grooves into a shape consisting of a trapezoid with an oval-shaped bottom. This will allow the foil edge to rest flush on a flat groove bottom. The current rebuild of the Astro-E mirror will use this modified groove design. These improvements and their effect on image quality are described in greater detail by Soong, Chan and Serlemitsos.²⁵

InFOC μ S is the first complete multilayer thin foil mirror capable of imaging with significant effective area in the 20–40 keV regime. Our flight demonstration of this mirror system shows great promise in opening up this poorly-explored part of the electromagnetic spectrum in our universe. Plans are in place to produce additional mirrors for InFOC μ S to cover the 65–70 keV energy band to observe the nuclear decay line of ^{44}Ti at 69.7 keV prominent in young supernova remnants. It will be necessary to improve both the interface roughness and stresses on the foils to accomplish this. Achievable improvements in the multilayer deposition process and alignment bar design will allow us to produce these additional mirrors and make exciting discoveries of the hard x-ray universe.

References

1. L.P. van Speybroeck, "Einstein Observatory /HEAO-B/ mirror design and performance" in *Space optics: Imaging X-ray optics workshop: Proceedings of the Seminar, Huntsville, Ala., May 22-24, 1979*, (Society of Photo-Optical Instrumentation Engineers, Bellingham, Wash. 1979), 2-11 (1979)
2. P.J. Serlemitsos, L. Jalota, Y. Soong, H. Kunieda, Y. Tawara, Y. Tsusaka, H. Suzuki, Y. Sakima, T. Yamazaki, H. Yoshioka, A. Furuzawa, K. Yamashita, H. Awaki, M. Itoh, Y. Ogasaka, H. Honda and Y. Uchibori, "The x-ray telescope on board ASCA," *Publ. Astron. Soc. Japan* **47**, 105-114 (1995)
3. G. Boella, R.C. Butler, G.C. Perola, L. Piro, L. Scarsi and J.A.M. Bleeker, "BeppoSAX, the wide band mission for X-ray astronomy." *Astron. Astrophys. Suppl. Series* **122**, no. 2, 299-307 (1997)
4. M.C. Weisskopf, H.D. Tananbaum, L.P. van Speybroeck and S.L. O'Dell, "Chandra X-ray Observatory (CXO): overview" in *X-Ray Optics, Instruments, and Missions III*, J.E. Truemper and B. Aschenbach, eds., Proc. SPIE **4012**, 2-16 (2000)
5. D.H. Lumb, H. Eggel, R. Laine and A.J. Peacock, "X-ray Multimirror Mission: an overview" in *EUV, X-Ray, and Gamma-Ray Instrumentation for Astronomy VII*, O.H. Siegmund and M.A. Gummin, eds., Proc. SPIE **2808**, 326-337 (1996)
6. H. Kunieda, M. Ishida, T. Endo, Y. Hidaka, H. Honda, K. Imamura, J. Ishida, M. Maeda, K.

- Misaki, R. Shibata, A. Furuzawa, K. Haga, Y. Ogasaka, T. Okajima and Y. Tawara, "X-ray telescope onboard Astro-E: optical design and fabrication of thin foil mirrors," *Appl. Opt.*, **40**, 553-564 (2001)
7. H.V. Bradt, R.E. Rothschild and J.H. Swank, "X-ray timing explorer mission," *Astron. Astrophys. Suppl. Series* **97**, 355-360 (1993)
8. C. Winkler, "The INTEGRAL Mission," *Exp. Astron.* **6**, 71-76 (1995)
9. G.R. Ricker, J.P. Doty, S.A. Rappaport, R.K. Vanderspek, M. Matsuoka, K. Nobuyuki, A. Yoshida, E.E. Feinmore, C. Ho and D. Roussel-Dupre, "The high-energy transient experiment (HETE) - An international multiwavelength mission" in *Gamma-ray bursts - Observations, analyses and theories*, C. Ho, R.I. Epstein and E.E. Feinmore, eds., (Cambridge Univ. Press, Cambridge, 1992)
10. O.S. Heavens and H.M. Liddell, "Staggered Broad-Band Reflecting Mirrors," *Appl. Opt.* **5**, 373-376, (1966)
11. F.E. Christensen, A. Hornstrup, N.J. Westergaard, H.W. Schnopper, J. Wood and K. Parker, "A graded d-spacing multilayer telescope for high energy X-ray astronomy" in *Multilayer and grazing incidence X-ray/EUV optics: Proceedings of the Meeting, San Diego, CA, July 22-24, 1991*, R.B. Hoover, ed., *Proc. SPIE* **1546**, 160-171 (1992)
12. B.D. Ramsey, C.D. Alexander, J.A. Apple, C.M. Benson, K.L. Dietz, R.F. Elsner, D.E. Engelhardt, K.K. Ghosh, J.J. Kolodziejczak, S.L. O'Dell, C.O. Speegle, D.A. Swartz and M.C.

- Weisskopf, "First Images from HERO, a Hard X-Ray Focusing Telescope," *Astrophys. J.* **568**, 432-435 (2002)
13. F.A. Harrison, S.E. Boggs, A.E. Bolotnikov, F.E. Christensen, W.R. Cook, W.W. Craig, C.J. Hailey, M.A. Jimenez-Garate, P.H. Mao, S.M. Schindler and D.L. Windt, "Development of the High-Energy Focusing Telescope (HEFT) balloon experiment" in *X-Ray Optics, Instruments, and Missions III*, J.E. Truemper and B. Aschenbach, eds., Proc. SPIE **4012**, 693-699 (2000)
14. J.A. Bookbinder, "Constellation X mission and its optics" in *X-Ray Optics for Astronomy: Telescopes, Multilayers, Spectrometers, and Missions*, P. Gorenstein and R.B. Hoover, eds., Proc. SPIE **4496**, 84-93 (2002)
15. K. Yamashita, P.J. Serlemitsos, J. Tueller, S. Barthelmy, L. Bartlett, K.-W. Chan, A. Furuzawa, N. Gehrels, K. Haga, H. Kunieda, P. Kurczynski, G. Lodha, N. Nakajo, N. Nakamura, Y. Namba, Y. Ogasaka, T. Okajima, D. Palmer, A. Parsons, Y. Soong, C. Stahle, H. Takata, K. Tamura, Y. Tawara and B. Teegardgen, "Supermirror hard x-ray telescope," *Appl. Opt.* **37**, 8067-8073 (1998)
16. W. Baumgartner, J. Tueller, S. Barthelmy, H. Krimm, F. Birsa and L. Ryan, "The CZT Pixelated detectors on the InFOC μ S hard x-ray telescope" in *New Century of X-Ray Astronomy*, H. Inoue and H. Kunieda, eds., ASP Conf. Series **251**, 520-521 (2001)
17. F.E. Christensen, A. Hornstrup, N.J. Westergaard, H.W. Schnopper, J.L. Wood and K. Parker, "A graded d-spacing multilayer telescope for high energy x-ray astronomy" in *Multilayer and Grazing Incidence X-ray/EUV Optics*, R.B. Hoover, ed., Proc. SPIE **1546**, 160-167

(1992)

18. Y. Soong, L. Jalota and P.J. Serlemitsos, "Conical thin foil x-ray mirror fabrication via surface replication" in *X-ray and Extreme Ultraviolet Optics*, R.B. Hoover and A.B. Walker, eds., Proc. SPIE **2515**, 64-69 (1995)
19. T. Okajima, K. Tamura, Y. Ogasaka, K. Haga, S. Takahashi, S. Ichimaru, H. Kito, S. Fukuda, A. Goto, K. Nomoto, H. Satake, S. Kato, Y. Kainata, A. Furuzawa, F. Akimoto, T. Yoshioka, K. Kondo, Y. Haba, T. Tanaka, K. Wada, N. Hamada, M. Hudaverdi, Y. Tawara, K. Yamashita, P.J. Serlemitsos, Y. Soong, K.-W. Chan, S.M. Owens, F. Berendse, J. Tueller, K. Misaki, R. Shibata, H. Mori, K. Itoh, H. Kunieda and Y. Nambu, "Characterization of the supermirror hard X-ray telescope for the InFOG μ S balloon experiment", Appl. Opt., submitted
20. K.D. Joensen, P. Voutov, A. Szentgyorgyi, J. Roll, P. Gorenstein, P. Hoghoj and F.E. Christensen, "Design of grazing-incidence multilayer supermirrors for hard x-ray reflectors," Appl. Opt. **34**, 7935-7944 (1995)
21. D. L. Windt, "IMD - Software for modelling the optical properties of multilayer films," Comp. in Phys. **12**, 360-370 (1998).
22. L. Nérot and P. Croce, "Caractérisation des surfaces par réflexion rasante de rayons X. Application à l'étude du polissage de quelques verres silicates," Rev. Phys. Appl. **15**, 761-779 (1980)
23. S.M. Owens, T. Okajima, Y. Ogasaka, F. Berendse and P.J. Serlemitsos, "Multilayer coated

thin foil mirrors for InFOC μ S" in *X-Ray Optics, Instruments, and Missions III*, J.E. Truemper and B. Aschenbach, eds., Proc. SPIE 4012, 619-625 (2000)

24. R. Shibata, M. Ishida, H. Kunieda, T. Endo, H. Honda, M. Kazutami, J. Ishida, K. Imamura, Y. Hidaka, M. Maeda, Y. Tawara, Y. Ogasaka, A. Furuzawa, M. Watanabe, Y. Terashima *et al.*, "X-Ray Telescope Onboard Astro-E. II. Ground-Based x-Ray Characterization," *Appl. Opt.* **40**, 3762-3783 (2001)
25. Y. Soong, K.-W. Chan and P.J. Serlemitsos, "Recent advance in segmented thin-foil X-ray optics" in *X-ray Optics for Astronomy: Telescopes, Multilayers, Spectrometers, and Missions*, P. Gorenstein and R.B. Hoover, eds., Proc. SPIE **4496**, 54-61 (2002)

Fig. 1. The InFOC μ S mirror. Each quadrant contains 255 nested pairs of thin foils in a conical approximation to a Wolter I configuration.

Fig. 2. Simulated reflectivity of foils over the radius range of the InFOC μ S mirror.

Foil 1 is at a radius of 5.89 cm and has 15 bilayers ranging from 15.35 nm (top) to 6.19 nm (bottom). Foil 151 is at a radius of 12.76 cm and has 50 bilayers ranging from 10.25 nm to 2.96 nm. Foil 255 is at a radius of 19.94 cm and has 60 bilayers ranging from 9.56 nm to 2.63 nm. The inner foils, with smaller angles of incidence, are designed to reflect the high-energy x rays while the outer foils reflect low-energy x rays. All simulations assume a layer interface roughness of 0.5 nm.

Fig. 3. Schematic view of the thin-film deposition chamber in top view (*a*) and side view (*b*). The chamber can contain up to 6 glass mandrels. The platinum and carbon targets are placed at opposite ends of the chamber. The small turntables, each holding one mandrel, rotate in front of the target to control the layer thickness. A large turntable holding the small turntables rotates the mandrels between the two targets. A mask in front of each mandrel compensates for non-uniform deposition rate along the vertical length of the mandrel.

Fig. 4. Schematic view of the reflectometer. A rotating anode x-ray source with a copper target produces x rays which are filtered with the double-crystal monochromator tuned to the Cu $K\alpha_1$ line at 8.047 keV. Collimation of the beam is performed by the 0.3×3 mm target spot size and a $120 \mu\text{m}$ diameter tantalum pinhole giving a divergence of 1.4 arcmin. The foils are rested on an "L" bracket to prevent foil bending. A 1 mm^2 CZT detector and the foil are rotated in a $\theta - 2\theta$ manner to determine the foil reflectivity.

Fig. 5. Reflectivity of Cu $K\alpha_1$ x rays (8.047 keV) vs. incidence angle (θ) for a typical foil. The variable parameters for the foil fits are the top-layer platinum, top-layer carbon, bottom-layer platinum, and bottom-layer carbon thickness and the interface roughness between layers. The fit degrades at large angles due to inaccurate layer thicknesses at the bottom of the graded d -spacing multilayer.

Fig. 6. Interface roughness vs. foil radius. The increased roughness for the larger foils is believed to be due to a buildup of roughness with increasing number of layers.

Fig. 7. Reflectivity vs. incidence angle (θ) of an inner group (*a*) and outer group (*b*) foil. Each is fitted with a best-fit interface roughness and the mean interface roughness of the outer (*a*) and inner (*b*) foils. All other parameters were allowed to vary to obtain the best fit.

Fig. 8. Ratio of measured to designed bilayer thickness vs. designed top bilayer thickness. The inner sample of foils, with higher bilayer thicknesses, are on the right side of the graph.

Fig. 9. Fitted vs. designed layer thickness ratios of platinum vs. carbon. The lack of a tight correlation between the top layer ratios eliminates systematic errors in the reflectivity measurement as the cause for the difference between measured and desired layer thickness. It also rules out common sources of systematic errors in the deposition process.

Fig. 10. The pencil-beam raster scan facility. An x-ray tube source is mounted on two 60-cm translation stages. The source is collimated by the source spot size of $105 \times 130\mu\text{m}$ and a $100\mu\text{m}$ tantalum pinhole at a distance of 0.7 m from the source giving a 1 arcmin divergence in the beam.

Fig. 11. The on-axis effective area of the complete InFOC μ S mirror. The models plotted in this figure are effective area calculations with no foil slope errors (solid) and a distribution of slope error similar to those on the Astro-E mirrors (dashed).

Fig. 12. Effective area vs. off-axis angle at 20 (solid), 30 (dashed), and 40 (dot-dashed) keV. The angles in this plot are offset in the azimuthal direction. The field of view of the telescope, defined as the full width at 50%, is 12.6, 10.5 and 9.3 arcmin at 20, 30, and 40 keV, respectively. Measured fields of view in the elevation direction were 9.0, 10.4 and 8.6 arcmin.

Fig. 13. Image produced by a raster scan over the entire mirror. The grayscale bar indicates the total number of counts in each detector pixel. The half-power diameter of this image is 3.0 arcmin, including systematic effects of the raster scan and binning into the 2.1×2.1 mm pixels.

Fig. 14. Encircled energy fraction of the raster scan image at 24 keV. The models in the figure are mirrors with different slope error distributions, labeled by the half-power diameter they produce at a given energy. Each model is folded into the systematic effects of the raster scan and binned into 2.1×2.1 mm pixels. Similar results were obtained at 28, 32 and 36 keV.

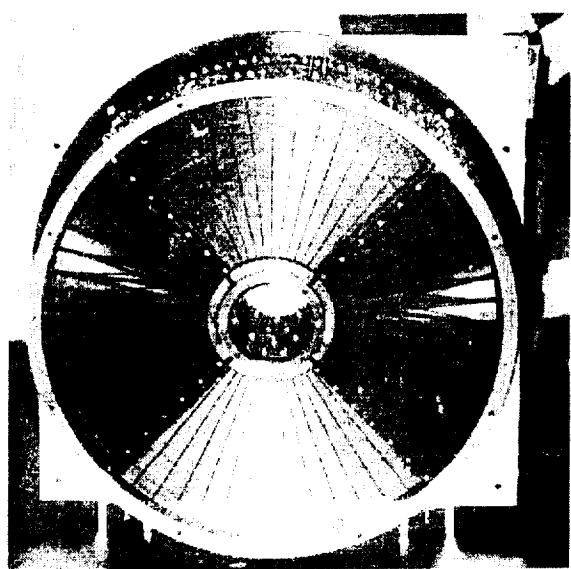


Fig. 1, Berendse et al.

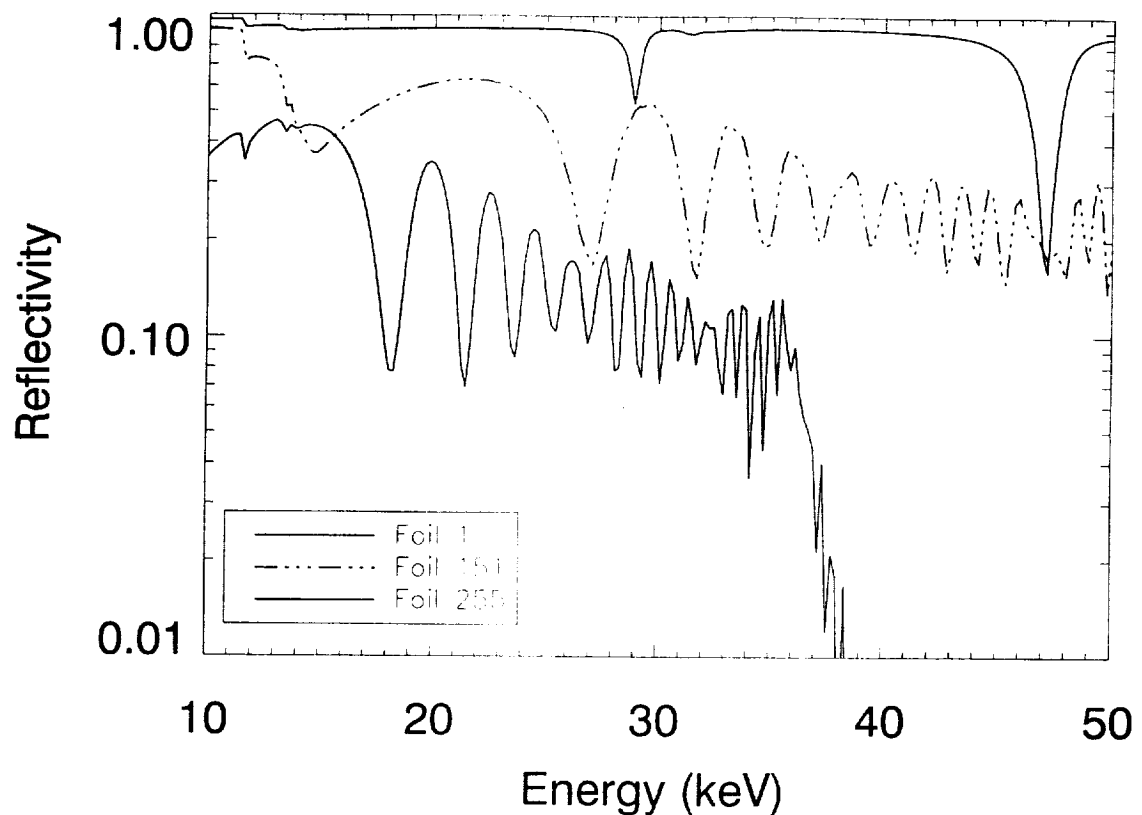
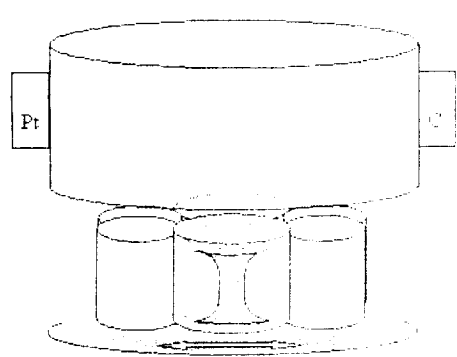
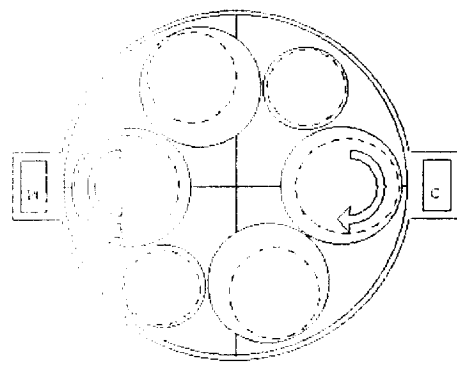


Fig. 2, Berendse et al.



3a.



3b.

Fig. 3, Berendse et al.

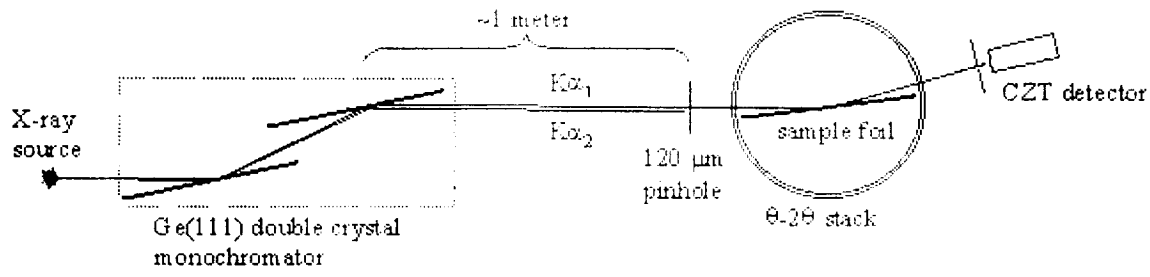


Fig. 4, Berendse et al.

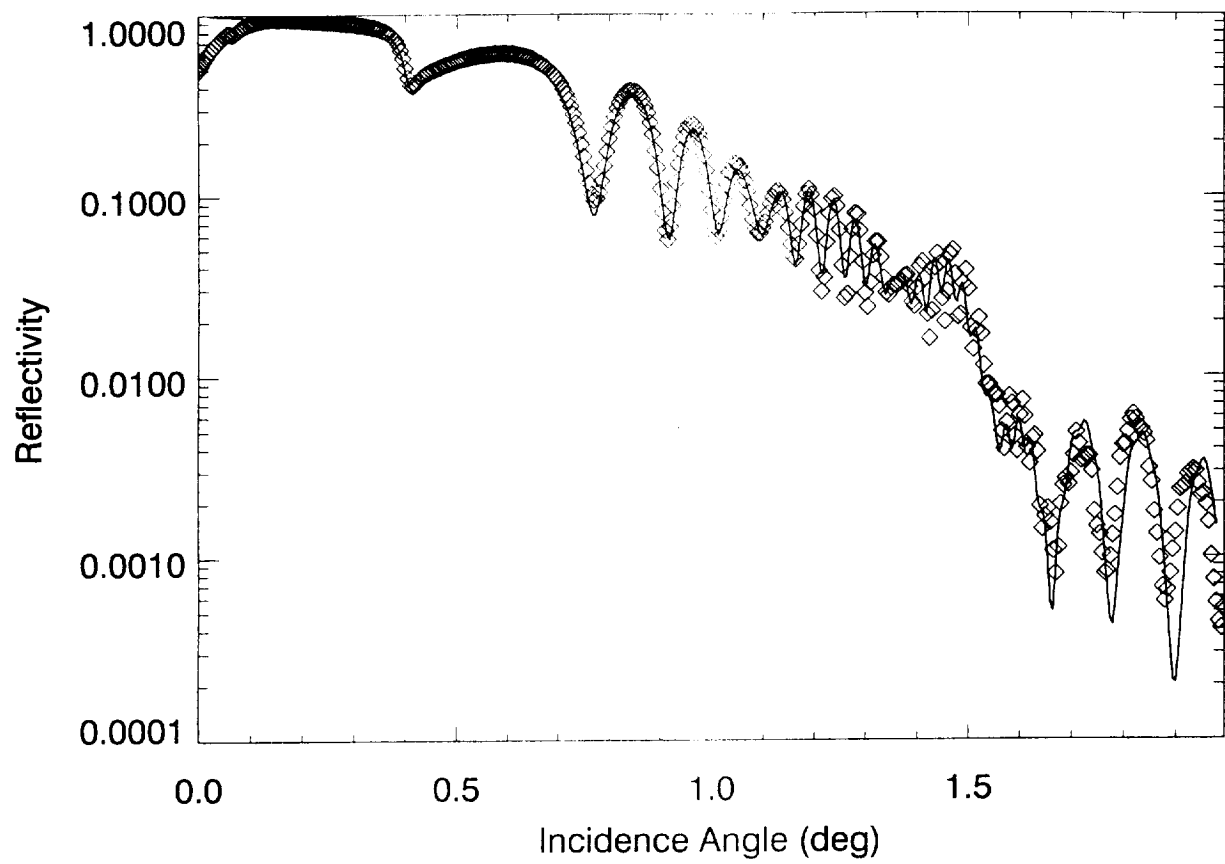


Fig. 5, Berendse et al.

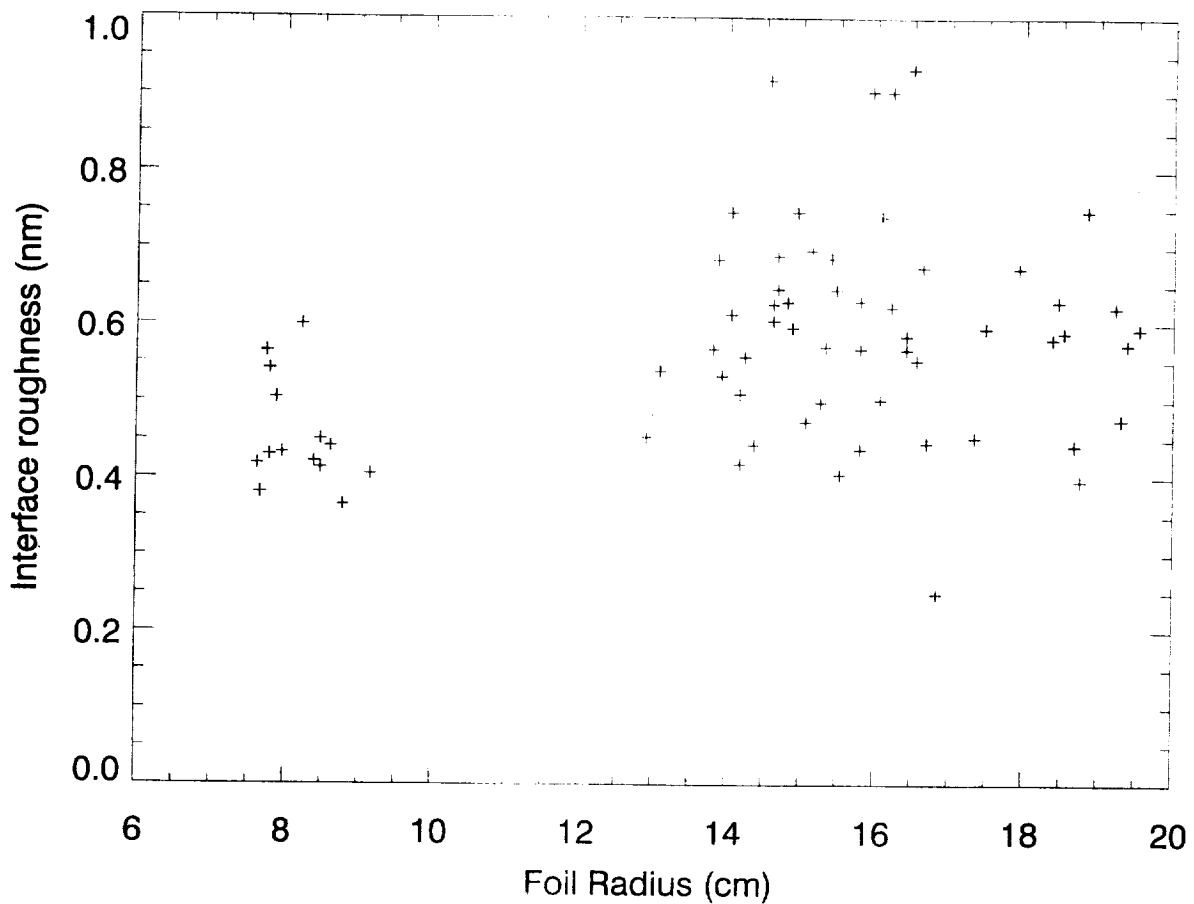
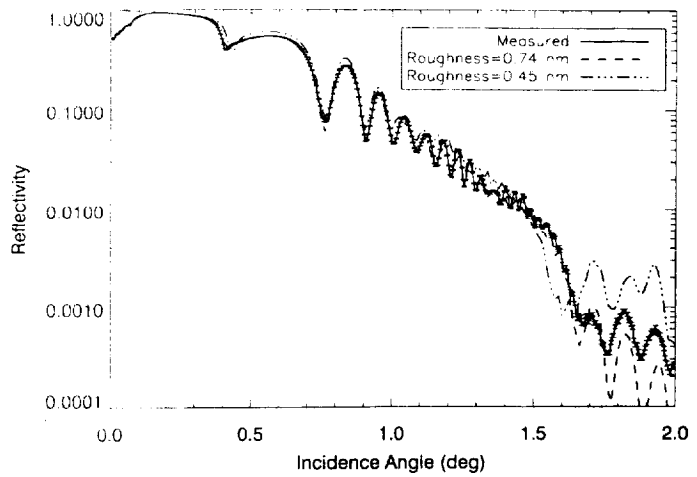
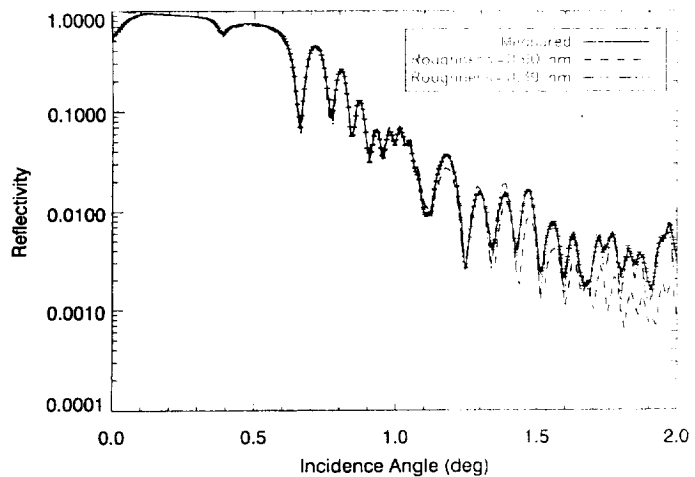


Fig. 6, Berendse et al.



7a.

7b.

Fig. 7, Berendse et al.

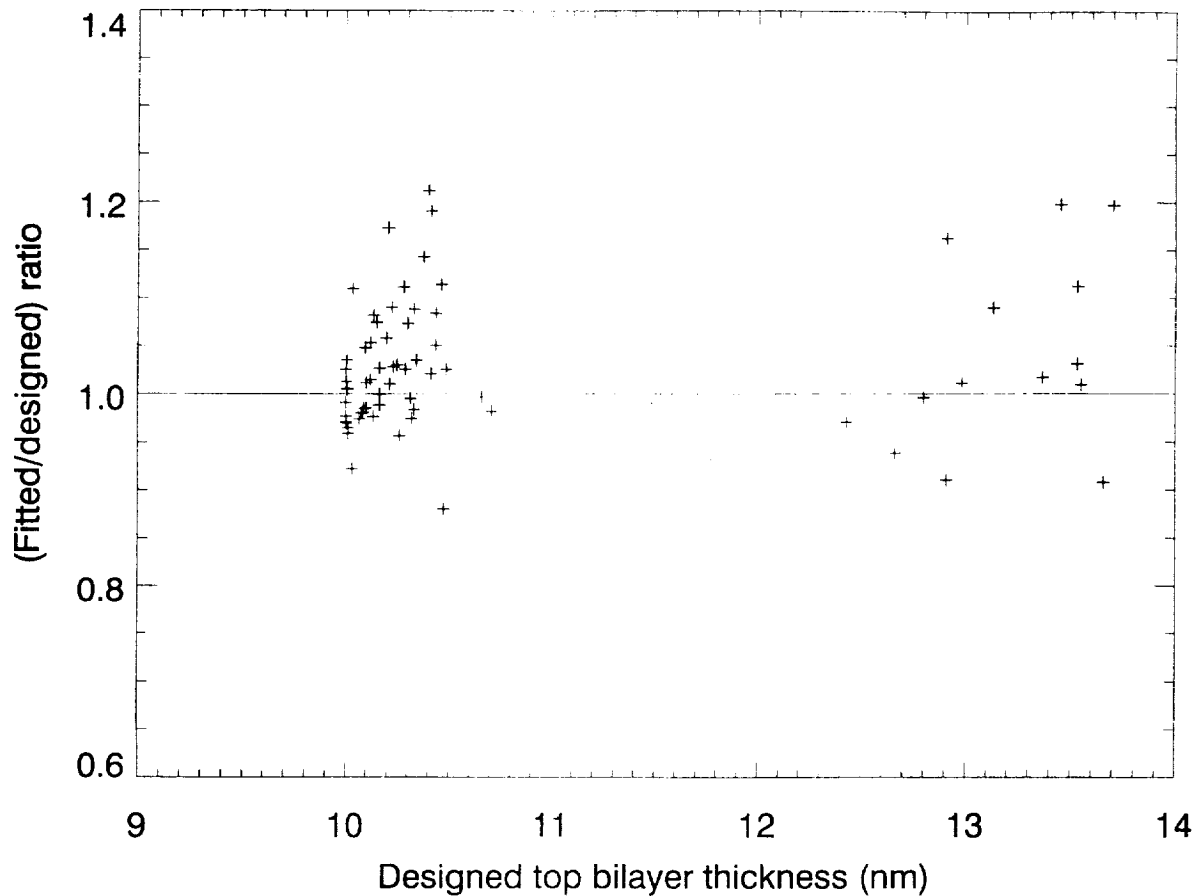


Fig. 8, Berendse et al.

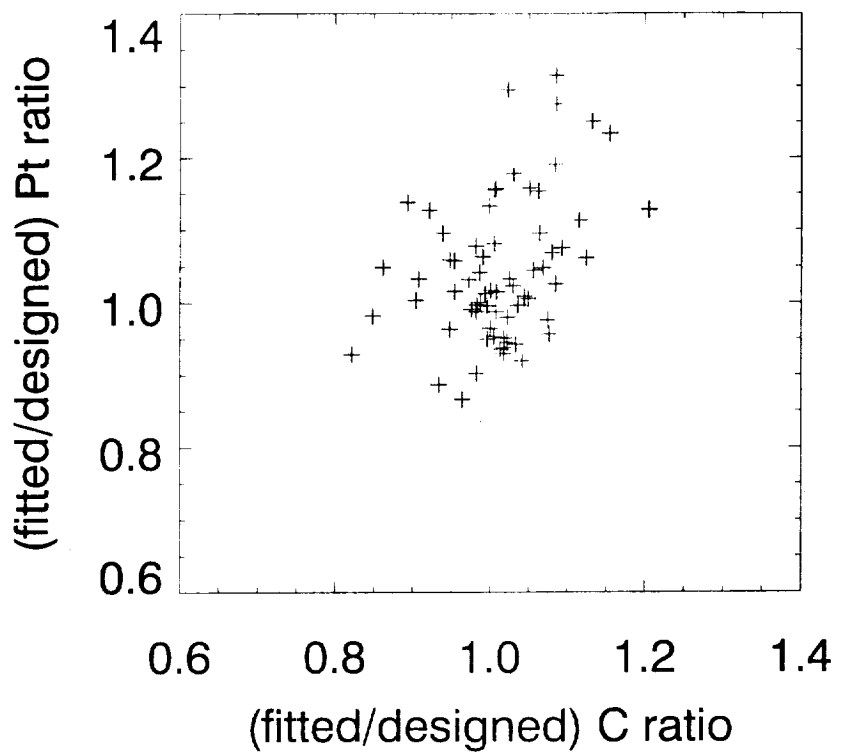


Fig. 9, Berendse et al.

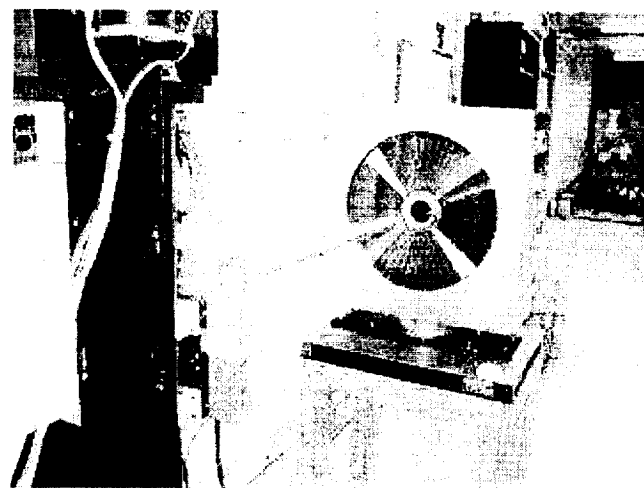


Fig. 10, Berendse et al.

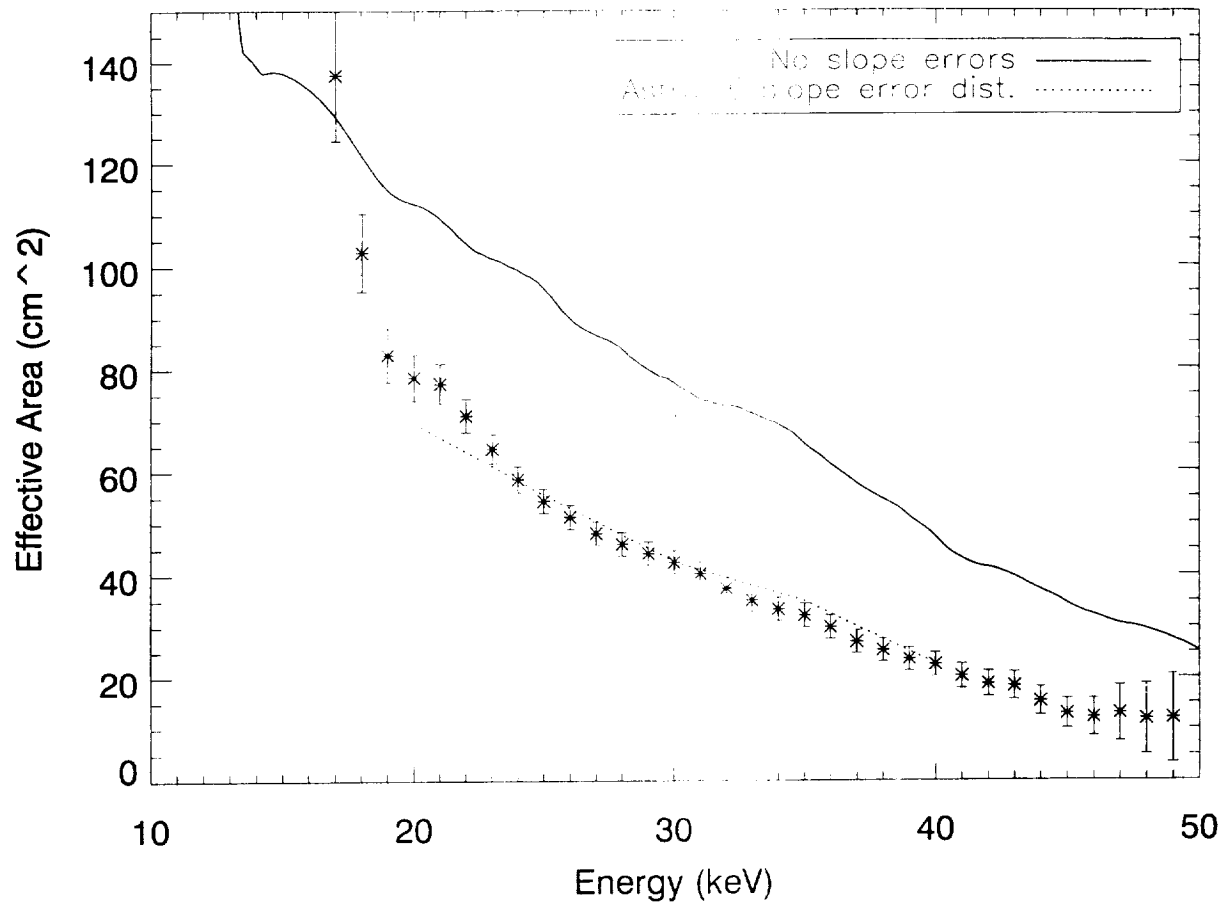


Fig. 11, Berendse et al.

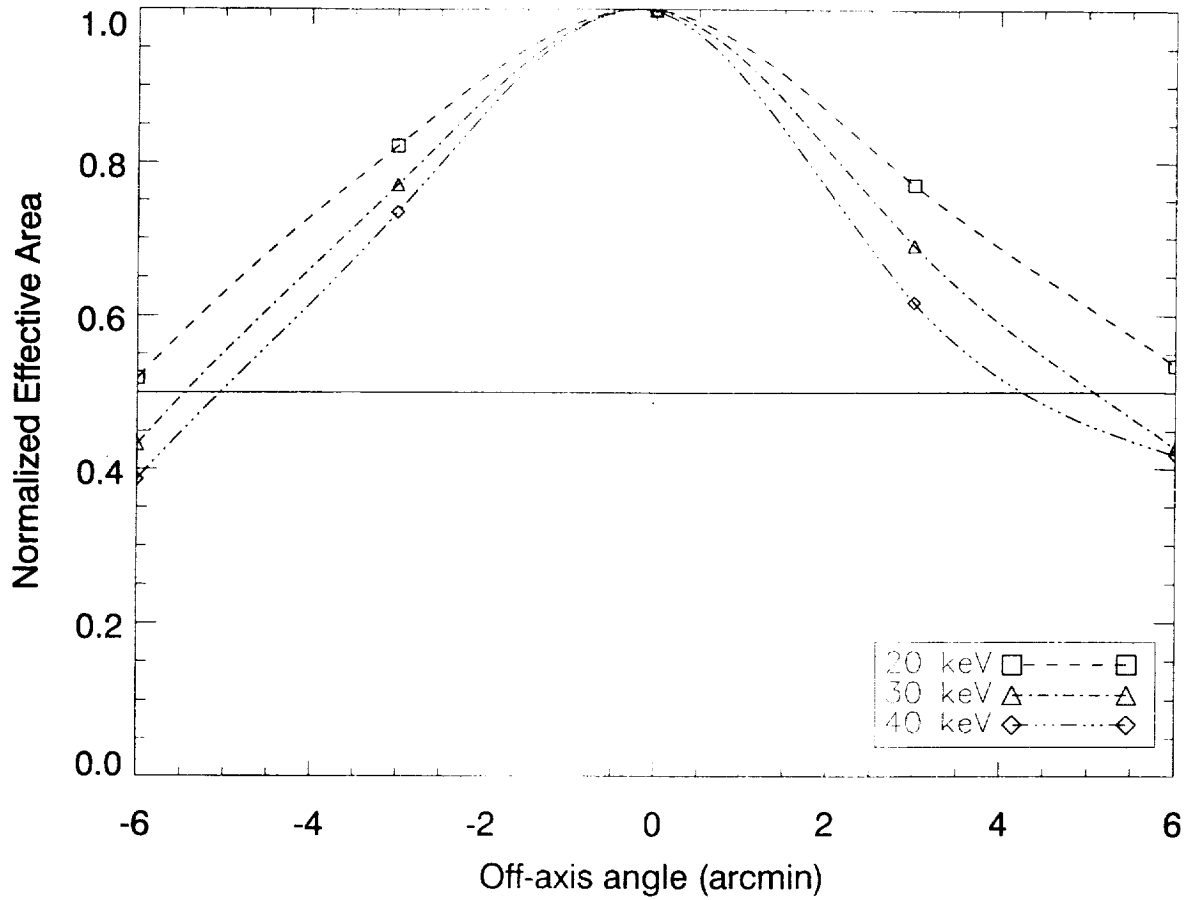


Fig. 12, Berendse et al.

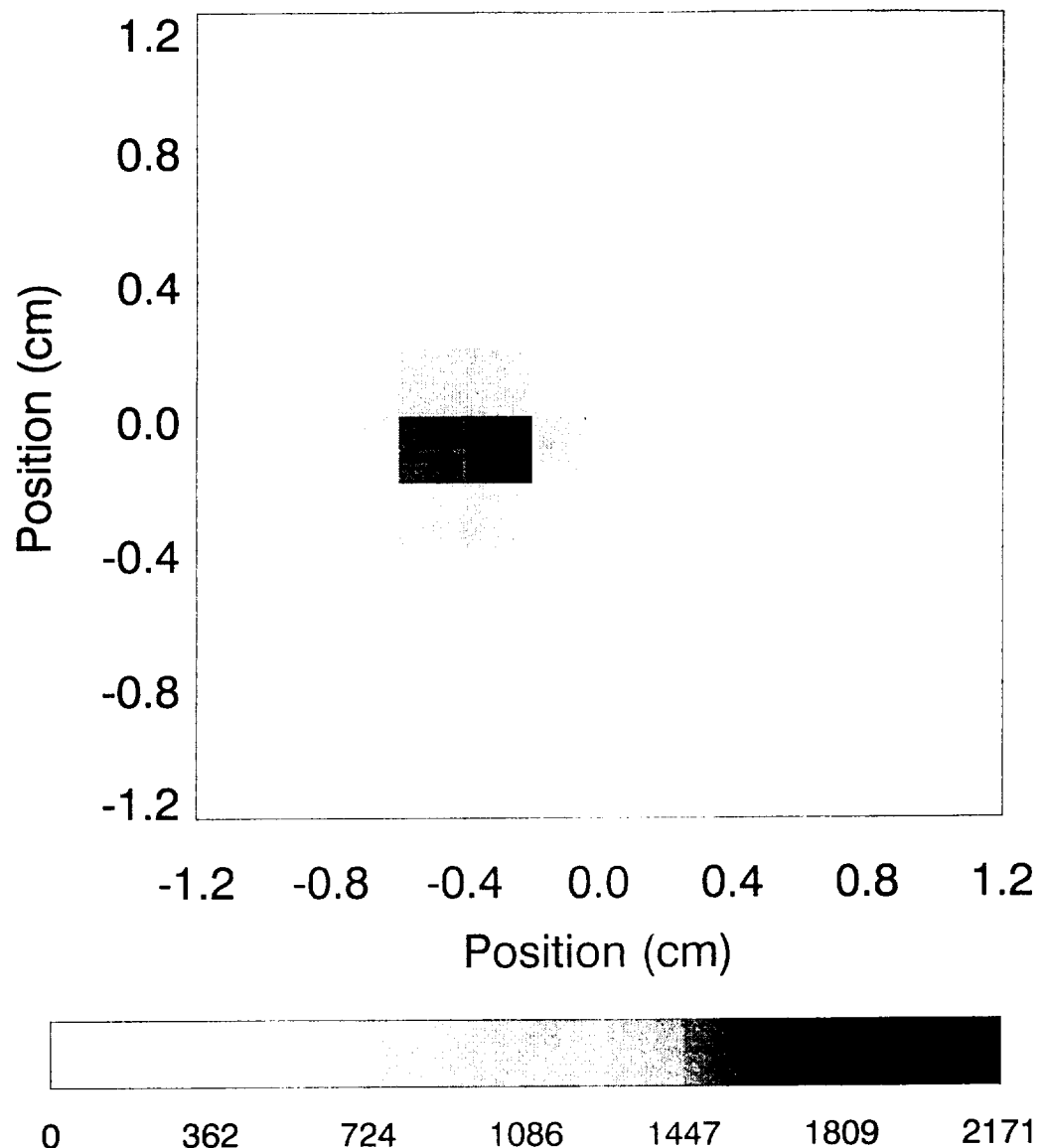


Fig. 13, Berendse et al.

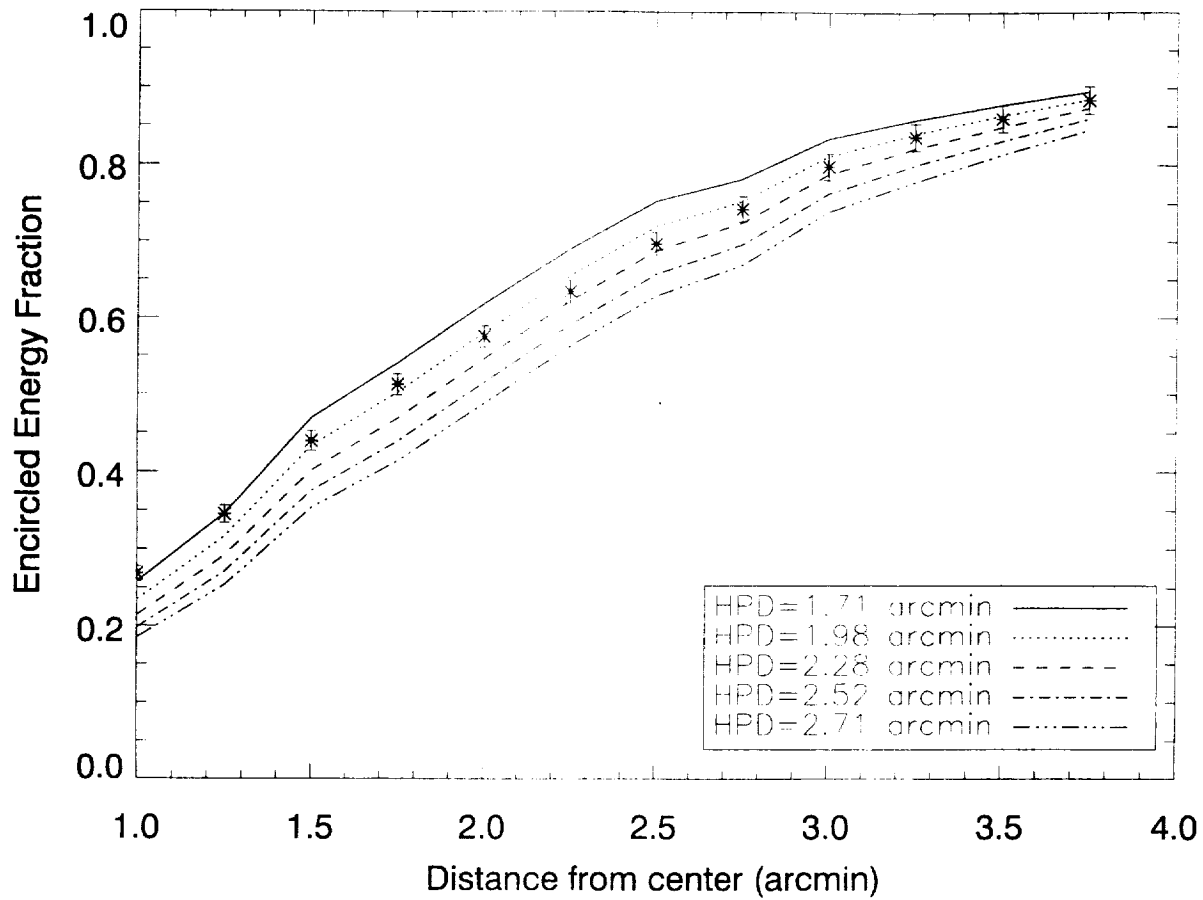


Fig. 14, Berendse et al.